Available online at www.sciencedirect.com
ScienceDirect
Trans. Nonferrous Met. Soc. China 32(2022) 175−191
Transactions of Nonferrous Metals Society of China
www.tnmsc.cn

Theoretical and experimental investigation of Ti alloy powder production using low-power plasma torches

Emre YURTKURAN[1], Rahmi ÜNAL[2]

1. Department of Mechanical Engineering, Faculty of Engineering and Natural Sciences, Sivas University of Science and Technology, Sivas, Turkey;
2. Department of Mechanical Engineering, Faculty of Engineering, Gazi University, Ankara, Turkey

Received 16 February 2021; accepted 26 September 2021

Abstract: This study was carried out to investigate the possibility of titanium alloy metal powder production using low-power plasma torches. An argon DC non-transferred arc plasma torch was designed, and numerical analysis was conducted to determine the plasma jet properties and wire temperature. The highest velocities inside the nozzle attachment were between 838 and 1178 m/s. The velocities of the jets at the apex were between 494 and 645 m/s for different gas flow rates. The studied plasma gas flow rates had no significant effect on the effective plasma jet length. It was shown that the plasma jet length can be estimated by numerical analysis using the temperature and velocity changes of the plasma jet over distance. It was observed that the powders produced were spherical without any satellites. As a result of this study, a plasma torch was developed and powder production was performed successfully by using relatively low torch power.

Key words: plasma atomization; particle size; powder production; thermal plasma torch; Ti alloy powder; computational fluid dynamics; microstructure

1 Introduction

There is a growing interest in additive manufacturing (AM) production technology. The success of these processes depends to a large extent on the availability and properties of powder materials [1]. Such powder materials need to be provided in the form of highly pure, fine, dense, and spherical powders [2,3]. Plasma atomization (PA) technology is one of the spherical powder production methods for titanium and its alloys. In recent years, this metal powder production technology has become an indispensable production technique for AM due to the superior properties of some powders such as their sphericity and flowability [4]. Plasma jets are able to both melt and atomize a material which is fed into the apex of jets in the form of a wire. The distribution of temperature and velocity in a plasma jet formed at the outer edge of plasma torches is very important in order to melt a solid wire and to disintegrate the liquid metal into fine spherical particles. Torch design is very important in providing a high jet velocity for an efficient atomization process. The plasma atomization process is based on the use of plasma torches generating plasma jets that converge towards an apex. The feed wire material is melted and atomized by the thermal and kinetic energy supplied by the plasma jets. Due to the physical size of such plasma torches, the apex of the plasma jets may be up to 5 cm away from the nozzle of the torches. The distance between the torch nozzle and apex varies according to the torch power [5] and the physical size of the plasma torch. This relatively long distance causes the loss of a considerable

Corresponding author: Emre YURTKURAN, Tel: +90-505-4623464, E-mail: yurtkuranemre@sivas.edu.tr
DOI: 10.1016/S1003-6326(21)65786-2

amount of thermal and kinetic energy in the plasma jets before they reach the apex position and touch the wire material [6]. LAROUCHE et al [5] operated each plasma torch at a power of 30 kW and an argon gas flow rate of 150 L/min. The values reported by TSANTRIZOS et al [7] were a total torch power of 83 kW and an argon gas flow rate of 100 L/min. It is possible to estimate the plasma jet properties by using numerical simulation to evaluate its suitability for plasma atomization with relatively low power. The plasma atomization method is especially important for powder production of refractory materials such as titanium and its alloys, but there is only a small amount of literature on plasma torches for powder production purposes. This study was carried out to investigate the possibility of metal powder production at low plasma torch power, and to determine the powder properties of the titanium alloy produced.

In this study, the plasma jet properties at the apex of three converging torches were estimated by numerical analysis to determine the production of metal powder at low plasma torch power. As a result of the numerical solutions, the powder production parameters were determined and applied in the experimental study. Titanium alloy powder production experiments were performed in a laboratory-scale plasma atomization system. The results of the numerical analysis and experimental studies were presented and discussed.

2 Experimental

Plasma atomization is a process in which a solid metal wire is melted and atomized at the apex of three plasma jets [8], as shown in Fig. 1(a). The plasma torch is one of the most important components of the system since it has a direct effect on the quality of the powders produced. In this process, plasma torches are DC non-transferred arc torches working with argon gas. The interior schematic view of the torches is shown in Fig. 1(b). The plasma gas flows through the small space between the cathode and the anode where the anode arc has a constrictive effect. As the gas flow continues, the plasma is formed by a high-voltage pulse that forms a conductive path for the electric arc between the cathode and the anode. The electric heating produced by the arc (Joule heating) causes the gas to reach very high temperatures (>10000 K). The expansion of the gas during the transition to the plasma state results in an acceleration of the plasma jet: the arc current interacts with its induced magnetic field and the Lorentz forces resulting from this interaction accelerate the gas. It also causes the formation of a cold boundary layer around the water-cooled anode wall. This layer is not electrically conductive and increases the temperature and velocity by narrowing the plasma jet. Thus, the plasma gas entering the torch at room temperature exits the torch in a plasma jet form at a very high temperature. The three torches are evenly placed around the central axis at 120° intervals, each forming an angle of 10° to 60° with respect to the vertical axis [5]. Plasma jets are able to melt the solid metal wire due to their high temperatures and disintegrate the metal into very small droplets (Fig. 1(c)) by the effect of the jet velocity. It is important that the three plasma torch combinations are positioned and the torch axes converge at an apex. It has been observed that this apex corresponds to the peak of the atomizing cutting forces of the plasma jet produced from the plasma torch. Properly positioned plasma torches expand the hot zone to provide the required temperature for the atomization process. Thus, the melting of the metal material by melting takes place more easily and efficiently. Although this situation does not have a direct effect on the sphericity of the produced powders, it has a positive effect on the sphericity as the droplets formed have sufficient temperature.

The torches used in this experimental study were designed according to the numerical analysis results and produced to very close tolerances. All connections (electricity, cooling water, and gas) were made behind the torch. The actual images of the PA system and some additional equipment where powder production was carried out are shown in Fig. 2. As shown in Fig. 2(a), the reactor with the upper wire feeding system was approximately 4.5 m in height. The reactor was evacuated by a vacuum pump and filled with argon gas to reduce oxygen inside the reactor. The wire was introduced through the wire feeding system shown in Figs. 2(b) and (d). The wire speed was adjusted via the controller shown in Fig. 2(c). Particle sizes of the atomized powders were measured, and the particle size distribution was

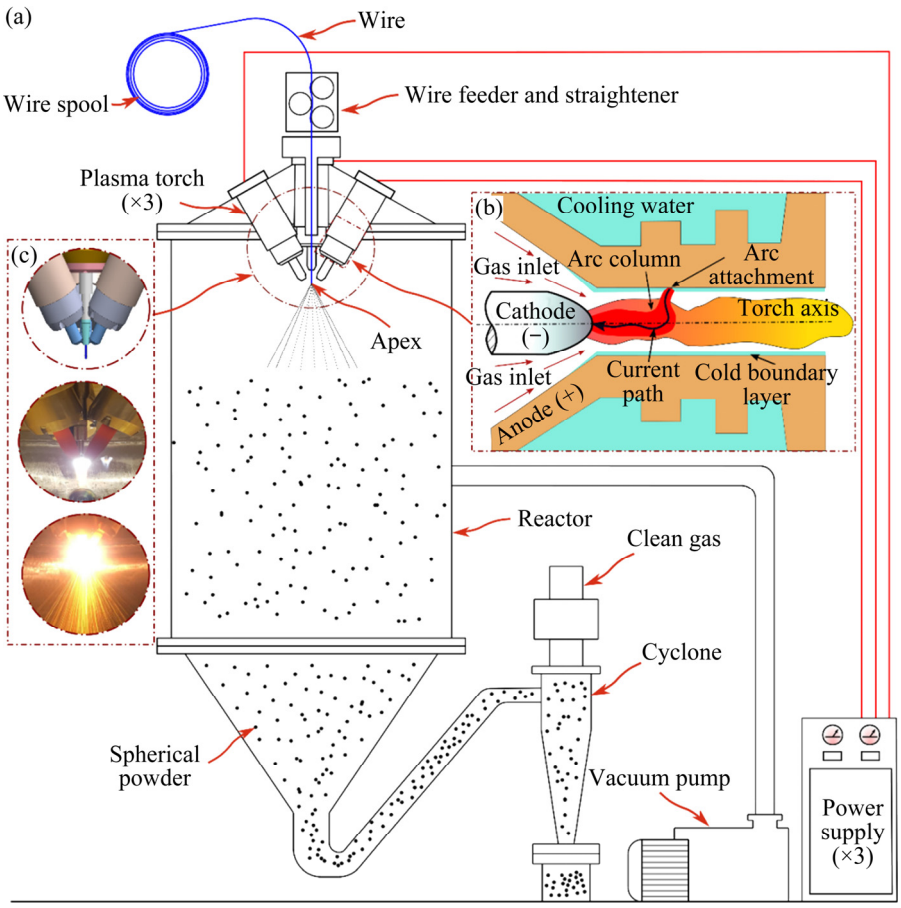

Fig. 1 Plasma atomization set-up: (a) General schematic view of system; (b) Internal schematic view of plasma torch; (c) Powder production image during operation

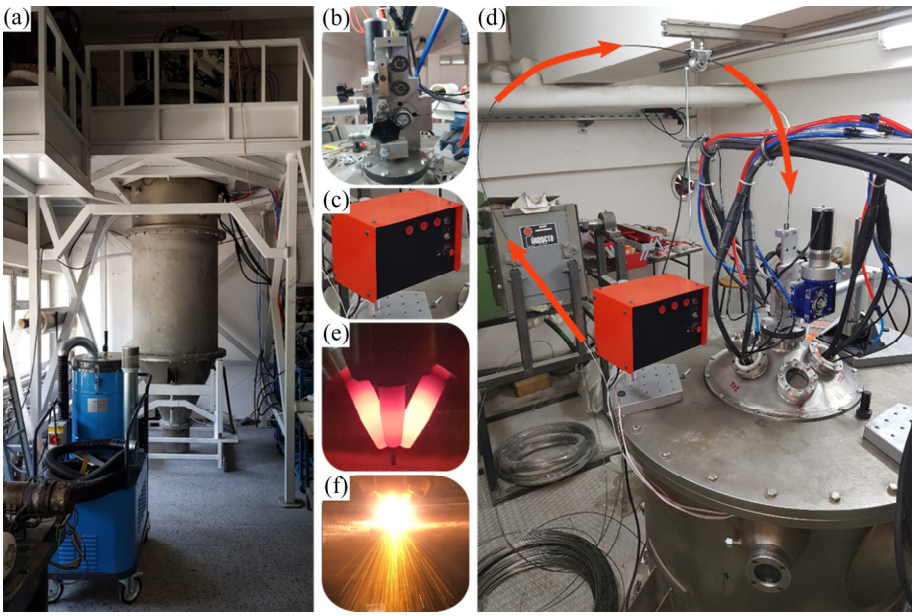

Fig. 2 Overview of PA reactor (a), wire feeder and straightener system (b), plasma ignition and wire speed controller (c), top view of reactor and torches (d), view of torches in reactor (e), and powder production (f)

obtained. The results were compared with similar powder information from published literature. Pore analysis of the internal structure of the powders was carried out by metallographic examination.

3 Theoretical method

3.1 Model assumptions

The following assumptions were made to model the plasma jet.

(1) The effects of gravity and viscous diffusion were neglected.

(2) Since the Mach number (*Ma*) at the nozzle inlets was generally 0.3 or less, the flow was considered incompressible. However, it is known that the flow at the torch exit was definitely subsonic flow ($0.3 < Ma < 0.8$) or supersonic velocity ($1.2 < Ma < 3$).

(3) Plasma was assumed to be in local thermodynamic equilibrium (LTE) to simplify the mathematical formulas. As a result, the plasma gas was considered to be a continuous fluid characterized by a single temperature.

(4) Plasma flow is considered steady-state and turbulent. Experimental studies conducted by the authors of this study and other researchers [9,10] on this subject revealed that the arc root attachment was fixed to one point and the area was eroded during long working periods. Accordingly, the steady-state assumption was feasible in determining the temperature and velocity values external to the thermal plasma torch. It also required the use of turbulence models (such as k−ε) due to the multi-scale structure of plasma flow within the thermal plasma torch. The arc caused the gas to heat up and expand rapidly. In this way, its acceleration increased and its flow became turbulent.

(5) The induced electric field is negligible.

(6) The plasma is optically thin. This assumption was made because the reabsorption of radiation was insignificant compared to the total radiation loss at all wavelengths.

(7) Only argon gas was used for the numerical analysis and experimental studies**.** It provided simplicity in modeling studies due to its simple chemical properties. It created an ineffective protective environment for the properties of the product in the material processes [11]. When used in the PA process, it did not react with liquid metal, and production was performed without pollution. Helium and other gases were not preferred because they increased costs. Nitrogen was not preferred as it forms nitrides. Air was not preferred because of its interaction with the tungsten cathode.

3.2 Governing equations

Modeling of plasma jets uses mass, momentum, and energy conservation equations. Also, modeling of arc formation involves Maxwell's electromagnetic equations. The flow is considered incompressible since Mach numbers at the torch inlet are usually 0.3 or less. However, arc formation and the convergent-divergent (CD) nozzle attachment cause the temperature and velocity values to increase. Thus, as a result of the increase in the Mach number, the flow passes into a compressible form. Ansys Fluent software performs the solution with compressible equations thanks to its adaptive solver feature. Therefore, the equations are given as compressible flow equations. These equations can be written according to Eqs. (1) to (8).

(1) Conservation of mass

$$\nabla\cdot\rho\boldsymbol{V}=0 \tag{1}$$

where ρ is the density; $\boldsymbol{V}$ is the gas velocity vector.

(2) Conservation of momentum

$$\rho\left(\boldsymbol{V}\cdot\nabla\boldsymbol{V}\right)=\boldsymbol{J}\times\boldsymbol{B}-\nabla p+\frac{2}{3}\mu\left(\nabla\boldsymbol{V}\right)+2\nabla\cdot\left(\mu\boldsymbol{S}\right) \tag{2}$$

where $\boldsymbol{J}$ is the current density vector; $\boldsymbol{B}$ is the magnetic induction vector; $\boldsymbol{J}\times\boldsymbol{B}$ is the Lorentz force; p is the pressure; μ is the dynamic viscosity; $\boldsymbol{S}$ is the strain rate tenser.

(3) Conservation of energy

$$\nabla\cdot\left(\rho\boldsymbol{V}h\right)=\nabla\cdot\left(\lambda\nabla T\right)+\boldsymbol{J}\times\boldsymbol{E}+\frac{5}{2}\frac{k_{\mathrm{B}}}{e}\boldsymbol{J}\cdot\nabla T \tag{3}$$

where h is the enthalpy; λ is the thermal conductivity; T is the temperature; $\boldsymbol{E}$ is the electric field; k_{B} is the Boltzmann constant; e is elementary charge.

(4) Maxwell electromagnetism and Ohm's law equations

$$\nabla\cdot\left(-\sigma\nabla\varphi\right)=0 \tag{4}$$

where σ is the electrical conductivity; φ is the electrical potential.

$$\boldsymbol{E}=-\nabla\varphi \tag{5}$$

$$\nabla^2\boldsymbol{A}=-\mu_0\boldsymbol{J} \tag{6}$$

where $\boldsymbol{A}$ is the magnetic vector potential; μ_0 is the permeability of free space.

$$\boldsymbol{B}=\nabla\times\boldsymbol{A} \tag{7}$$

$$\boldsymbol{J}=\sigma\boldsymbol{E} \tag{8}$$

The gas entering the plasma torch suddenly

warms up due to arc formation. The arc causes the gas to heat up and expand rapidly. In this way, its acceleration increases and its flow becomes turbulent. Therefore, the k–ε turbulence model was used. The turbulence kinetic energy, k, and its rate of dissipation, ε, were obtained from the following transport equations (Eqs. (9) and (10)).

$$\nabla\cdot(\rho k v)=\nabla\cdot\left[\left(\mu+\frac{\mu_t}{\sigma_k}\right)\nabla k\right]+G_k-\rho\varepsilon \quad (9)$$

$$\nabla\cdot(\rho\varepsilon v)=\nabla\cdot\left[\left(\mu+\frac{\mu_t}{\sigma_\varepsilon}\right)\nabla\varepsilon\right]+\frac{\varepsilon}{k}(C_{1\varepsilon}G_k-\rho\varepsilon C_{2\varepsilon}) \quad (10)$$

where v is the velocity; μ_t is the turbulent viscocity; G_k represents the production of turbulent kinetic energy and is modeled identically for the standard, RNG, and realizable k–ε models. The terms σ_k and σ_ε are the turbulent Prandtl numbers for k and ε, respectively; $C_{1\varepsilon}$ and $C_{2\varepsilon}$ are constants, and the values entered into the ANSYS simulation program in this study were as follows: $C_{1\varepsilon}$=1.44, $C_{2\varepsilon}$=1.92, C_μ=0.09, σ_k=1 and σ_ε =1.3. The exact equation for the term defined for the transport of k, is shown in Eq. (11):

$$G_k=-\rho\overline{v_i'v_j'}\nabla_v \quad (11)$$

where v_i' and v_j' are the mean and fluctuating velocity components, respectively; $-\rho\overline{v_i'v_j'}$ is Reynolds stress; ∇_v is the $\partial v_i/\partial x_i$.

The turbulent viscosity, μ_t is computed by combining k and ε in Eq. (12):

$$\mu_t=\rho C_\mu(k^2/\varepsilon) \quad (12)$$

where C_μ is a constant.

3.3 Boundary conditions and computational domain

Figure 3(a) shows modeling elements and representation of data receiving lines. A mesh structure and computational domain were used to simulate the PA system as shown in Fig. 3(b). The wire diameter was 3 mm. In order to accelerate the analysis studies, a 120° section was modeled. The computational domain included the anode, the cathode region (Fig. 1(b)), and the high velocity nozzle attachment that accelerated the plasma jet to the apex. The apex point is shown in Fig. 1(a) and the torch nozzle was as close as possible to the apex. However, this was not possible due to the physical dimensions of the torches. For that reason, a nozzle attachment was assembled onto the torches. Thus, the distance between the apex and torch nozzle was reduced to 20 mm.

The maximum skewness value of the mesh elements was 0.77, and the minimum orthogonal quality value was 0.23. Mesh sensitivity tests were performed to increase the reliability of the simulation results. For these tests, the changes in

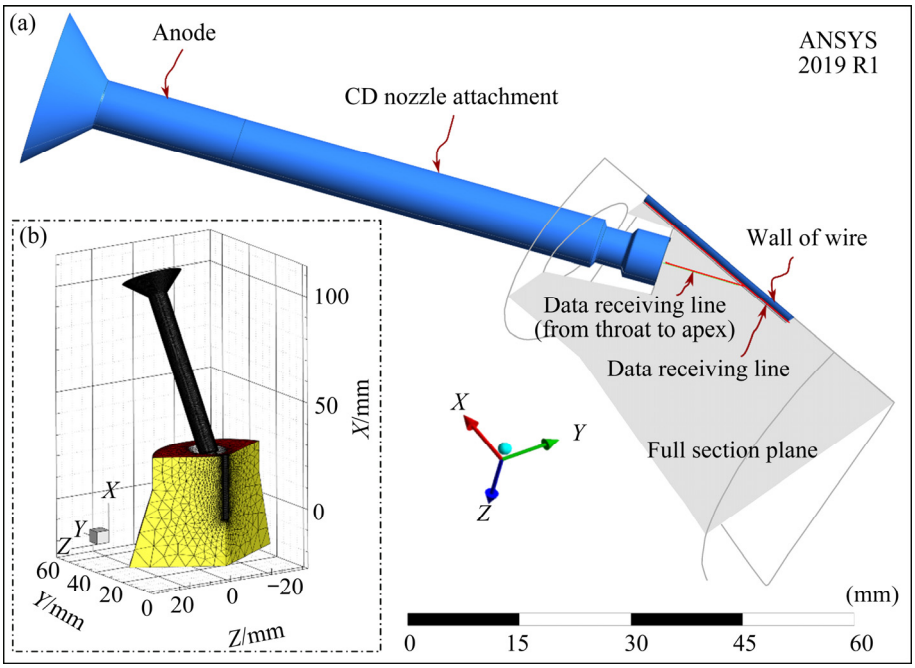

Fig. 3 Modeling elements and representation of data receiving lines (a), and geometry of computational domain and mesh structure (b)

the average temperature and velocity values in the exit cross-section of the torch were examined. It was observed that the average temperature and velocity values did not change after approximately 90000 cell numbers, and cell numbers ranging from 90000 to 130000 were used in modeling processes. Values such as thermal and electrical conductivities and the enthalpy of argon gas from low temperatures to high temperatures were taken from Ref. [12] to fully simulate the thermal and electrical behavior of the argon gas at high temperatures (30000 K). Argon gas entered axially into the plasma arc region. Ti−6Al−4V alloy wire material properties were compiled from Ref. [13] and defined in the software. Modeling was carried out using ANSYS Fluent software with the magnetohydrodynamics (MHD) module, which was used to solve the relationship between the electromagnetic field and the gas flow. Plasma applications such as plasma atomization require supersonic flow with a high Mach number to produce finer powder sizes. The k–ε model with coupled algorithm and second-order upwind were used to obtain a reliable solution. Other solution algorithms diverged due to both the high Mach number and the sudden rise in temperature during the plasma formation process.

The main purpose of the numerical analysis was to determine the temperature of the wire at the apex region for melting purposes. The data receiving lines are shown in Fig. 3(a). The first data line was at the center of the torch starting from the throat of the nozzle attachment up to the apex. The second data line was parallel to the wire direction and was shifted 0.5 mm from the wire surface. The temperature distribution on the surface of the wire was estimated by using the second data line and it was discussed in relation to melting.

The boundary conditions used for the computational domain are shown in Table 1. The values given in this table are the same as those used in the experimental studies. For example, gas inlet and cathode temperatures were determined to be 300 K. By entering the anode thickness, the cooling water temperature was defined as 300 K. The anode material was copper, and the cathode material was tungsten alloy with 2% Th. On the cathode tip surface, a Gaussian-like current density profile $J(r)$ was imposed and defined as follows:

$$J(r)=J_0\exp\left[-\left(r/R_c\right)\right]^{n_c} \tag{13}$$

where J_0 represents the maximum electric current density at the cathode tip; r is the radial distance from the torch axis; R_c is the are core radius; J_0 and n_c are parameters that specify the shape of the current density profile. The maximum current density was $J_0=2.1\times10^8$ A/m^2 , where n_c was 5 and the value of R_c was chosen to ensure that the integration of $J(r)$ over the cathode tip area was equal to the total applied current of 300 A.

Table 1 Boundary conditions for computational domain

Position	Pressure, p/MPa	Temperature/ K	Gas flow rate/ (L·min^{-1})	Current density/ (A·m^{-2})
Inlet	0.3	300	60, 70, 90	$\partial J/\partial n=0$
Cathode	$\partial p/\partial n=0$	300	0	$J(r)$
Anode	$\partial p/\partial n=0$	$\partial T/\partial n=h_{conv}$	0	$\partial J/\partial n=0$
DG addition	$\partial p/\partial n=0$	$\partial T/\partial n=h_{conv}$	0	$\partial J/\partial n=0$
Wire	$\partial p/\partial n=0$	$\partial T/\partial n=h_{conv}$	0	$\partial J/\partial n=0$
Outlet	0.1	$\partial T/\partial n=h_{conv}$	$\partial V/\partial n=0$	$\partial J/\partial n=0$

n is real number (text) and normal to boundry; h_{conv} is convective heat transfer coefficient

4 Results and discussion

4.1 Comparison of experimental visible plasma jet with numerical solution

Plasma jet outlet temperatures were above 10000 K. In order to determine the reliability of the analysis results, the torches were kept at 300 A and run individually at plasma gas flow rates of 60, 70, and 90 L/min. The effect of the plasma gas flow rate on the plasma jet properties and the comparison with the experimental images are shown in Fig. 4. For the comparison process, the lowest (299.9 K) and the highest (32210.4 K) temperatures in the temperature distribution scale were applied to all gas flow rates. Since all measurements were known, the resulting temperature distribution graph was compared with the actual plasma jet images of the torch. Line No. 1 in Fig. 4 indicates where the anode ended and the high velocity nozzle attachment started. Line No. 2 in Fig. 4 denotes the location of the high velocity nozzle attachment point. Point 3 shows the output point of the torch. The graphs were drawn over a 25 mm distance starting at the torch output point (Point 3) and ending at Point 4. In addition, these numbers are also shown on the temperature and velocity graphs. By using the images in Fig. 4, the visible length of

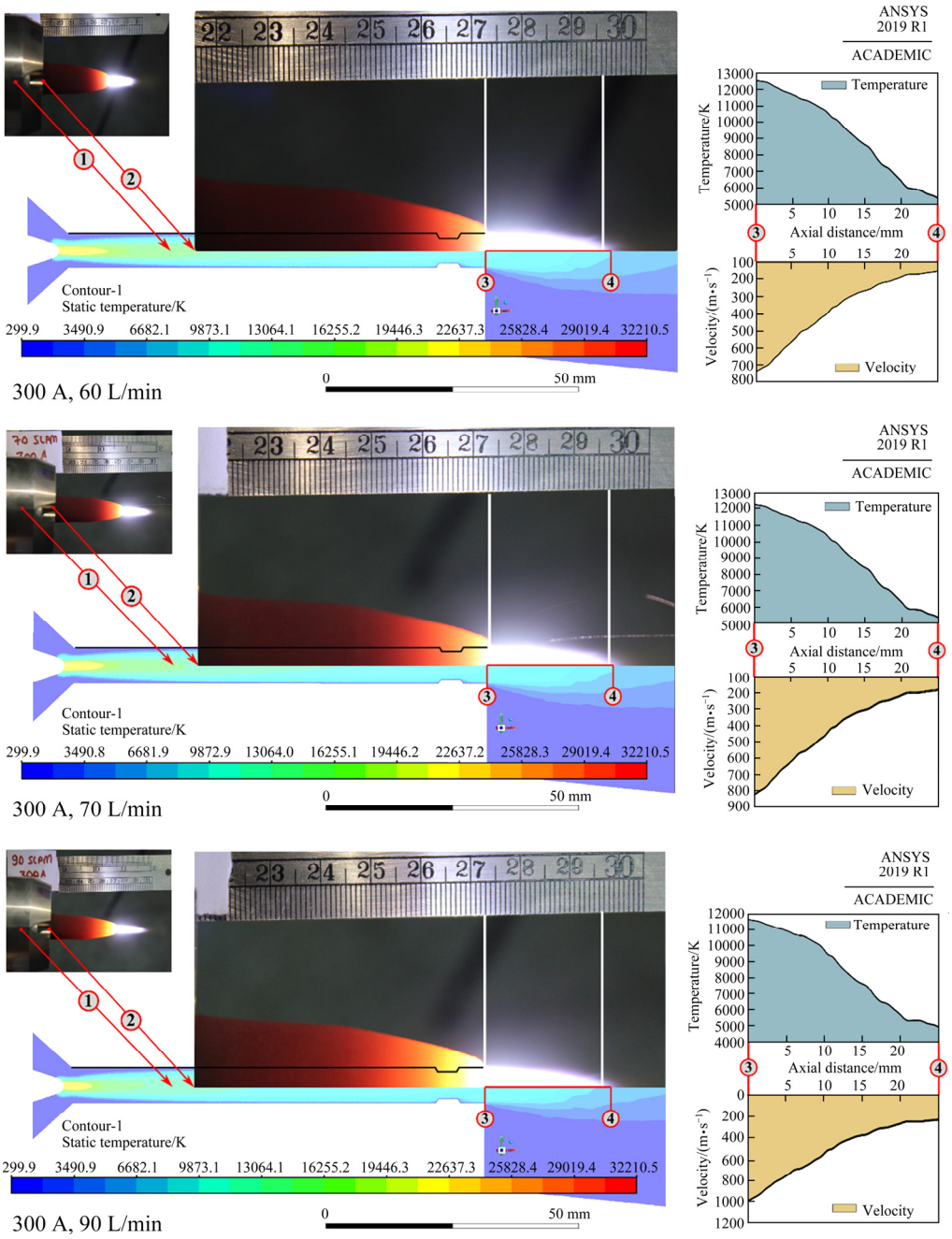

Fig. 4 Effect of mass flow rate on plasma jet properties and comparison with experimental images

the plasma jets was determined. The temperature and velocity graphs showed a distinct change at a specific distance from the torch nozzle and this point may be evidence of the endpoint of the visible plasma jet. In particular, the visible jet length measured for 300 A and 70 L/min and the jet length obtained from the numerical analysis were comparable to each other. The visible jet length determined experimentally for all flow rates was approximately 23 mm. By determining the recognizable change points on the graphs, it was possible to estimate the jet lengths by using the temperature and velocity graphs. It was seen that this distance was approximately 22 mm. These results may be considered as confirmation of this approach.

The experimentally measured voltage values for each of the plasma torches for these 3 flow rates were in the range of 26 to 30 V. The generated power value for each torch was calculated to be approximately 9 kW. In Refs. [5] and [7], powder production was accomplished using the power of 20 to 40 kW per torch. In this study, it was shown that spherical and fine powders can be produced

with a lower torch power. Thus, we can conclude that it is possible to produce Ti alloy powder by using lower power.

4.2 Solution for wire temperature and velocity

The total current value of 300 A was kept constant, and 60, 70, and 90 L/min gas flow rate values were used for numerical analysis. The distance of the data line parallel to the wire direction was 30 mm. Temperature and velocity values were taken from the points on a line 0.5 mm away from the wire surface and the results are given in Fig. 5. Accordingly, when the velocity values were examined, the highest values occurred at the apex. The highest temperatures occurred at approximately 10 mm above the apex. This result showed that unless a suitable wire velocity is selected powders having a coarser powder size will be produced compared to powders produced at the apex. In terms of variables, the highest velocity was obtained for 90 L/min at 300 A. The highest temperature was obtained at a gas flow rate of 60 L/min. As a result of the analysis made at gas flow rates of 60, 70, and 90 L/min, velocity values at the apex were 489.1, 539.51, and 643.31 m/s, respectively. Temperatures at the apex for these flow rates were 11575.89, 11234.42, and 10636.32 K, respectively. These results showed that the plasma jet temperature and velocity values are enough for the plasma atomization of the Ti alloy. These values are point values taken from modeling studies. In addition, making an inference only from high temperature values may cause wrong results. It should be evaluated together with the velocity values occurring in the apex area. The velocity values obtained from the apex are 489.10, 539.51, and 643.31 m/s. When the temperature and velocity values are examined together, the melting and atomization processes in the plasma atomization process occur simultaneously. This situation leads to the conclusion that the material in solid form atomizes and solidifies before it has time to evaporate (or evaporates at a negligible level).

4.3 Temperature and velocity profiles

Figure 6 shows the temperature and velocity graphs drawn with data taken from a line between the nozzle throat point and the apex. Accordingly,

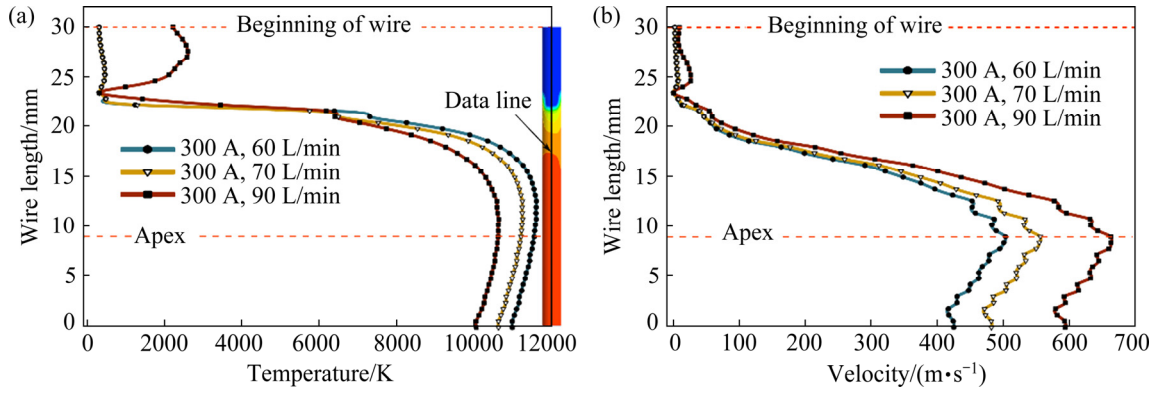

Fig. 5 Comparison of temperature (a) and velocity (b) values for plasma jet

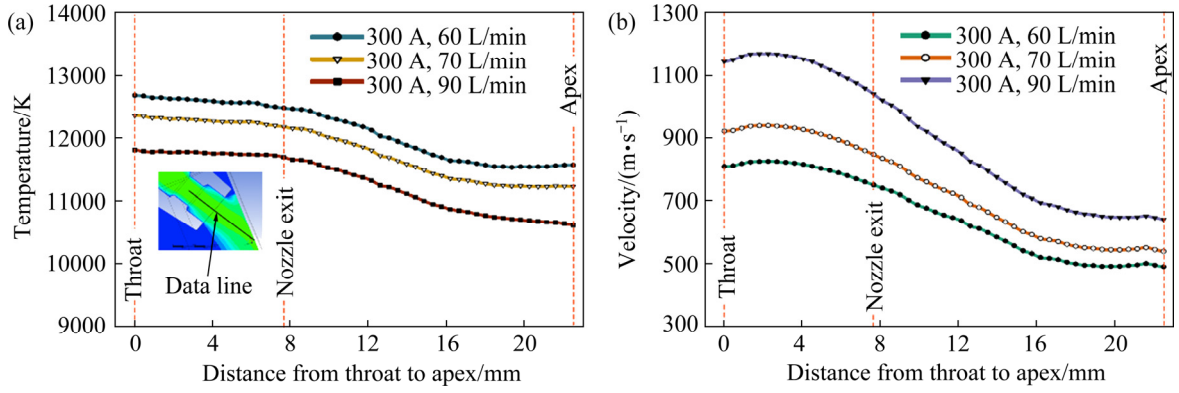

Fig. 6 Comparison of temperature (a) and velocity (b) from nozzle throat to apex

the drop in temperature values from the torch nozzle exit is negligible, considering the melting temperature of the wire. The decrease in velocity is more noticeable. Velocity values between the nozzle exit and apex at gas flow rates of 60, 70, and 90 L/min are decreased by 35%, 37%, and 39%, respectively.

The temperature and velocity distributions under operating conditions are shown in Fig. 7. Accordingly, the highest temperatures occurred at very close distances to the cathode tip. The maximum temperature ranged from 25942 to 32515 K. The velocity reached the highest value on the throat section. The highest velocities inside the nozzle attachment were between 838 and 1178 m/s. The velocities of the jets at the apex were between 494 and 645 m/s for different gas flow rates.

The PA process requires high-temperature values to melt the wire and high-velocity values to atomize the melt. The elevated temperatures obtained at the intersection of the plasma jets were sufficient to melt a Ti−6Al−4V alloy wire. The temperature values obtained according to Fig. 5 mean that the wire start to melt before reaching the apex. The temperatures are above the melting temperature of the metal wire. In order to create a strong atomization environment, high-velocity values are also needed. The velocity values of the jets are the highest at the apex. In order to produce powders of fine size, disintegration should be carried out at the highest possible velocity. Accordingly, it has been inferred that when a suitable wire velocity is selected, the melting and atomization processes will take place simultaneously at the apex, and powders of a fine size will be produced.

4.4 Shape, size, and microstructure of powders produced

At the conclusion of the numerical modeling studies, it was decided to use parameters of 300 A and 90 L/min in the experimental study. Powder production using this parameter set was performed, as shown in Fig. 8. Figure 8(a) shows the image

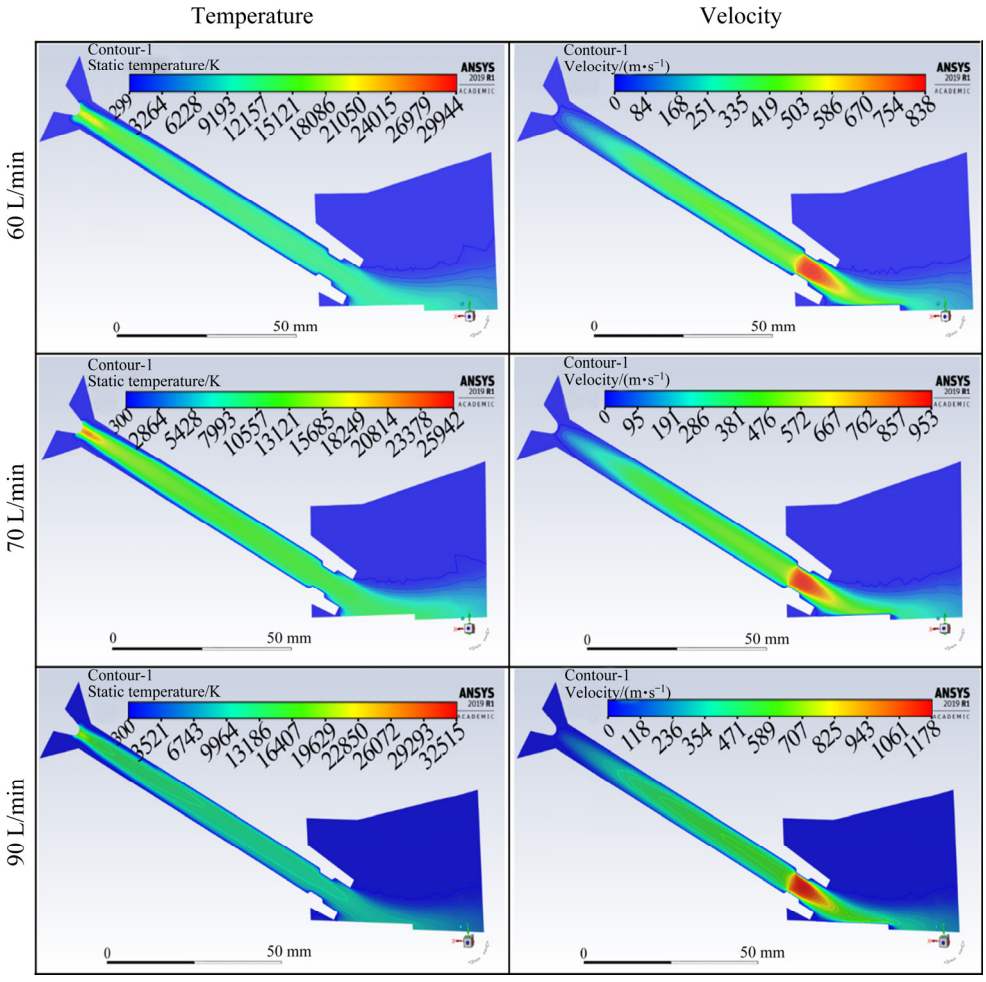

Fig. 7 Temperature and velocity profiles at gas flow rates of 60, 70, and 90 L/min

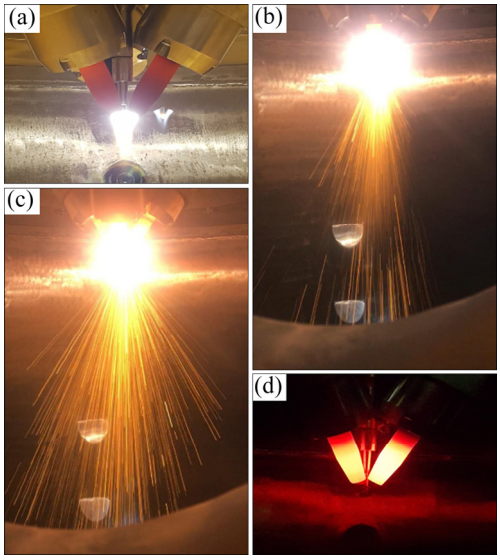

Fig. 8 Plasma atomization images during powder production: (a) Before wire feeding; (b, c) During production; (d) Immediately after production

before wire feeding, Figs. 8(b) and (c) show the moment of powder production, and Fig. 8(d) shows the image after production. It was concluded from the experimental study that the symmetry of the torch positions is very important. If one of the torches works irregularly, the melt will shift towards the torch side, and the atomized particles will solidify before they can attain their spherical shape.

The shape and oxygen content of the powder particles are important to obtain the properties required for AM and conventional powder metallurgy processes. Minimizing the oxygen level before starting production is effective on the oxygen levels of the produced powders. The oxygen content of the produced powders was 0.011−0.035 wt.%. In order to carry out the described characterization processes, the classification of the particles was carried out in two size ranges: 0 to 53 μm and 53 to 125 μm. Particle size distribution analysis was performed by using SEM images.

Figure 9 shows SEM images at various magnification scales for the powder particles in the 0−53 μm size range and their particle size distribution curve. It is seen that almost all of the powder particles have a perfectly spherical shape. In general, it is desirable that the spheroidization time for liquid droplets should be smaller than the solidification time in order to produce spherical powders [14], and that a short spheroidization time is achieved with low liquid metal viscosity. High surface energy and small particle size contribute to spherical particle formation before solidification. Thus, it can be concluded from the shapes of the

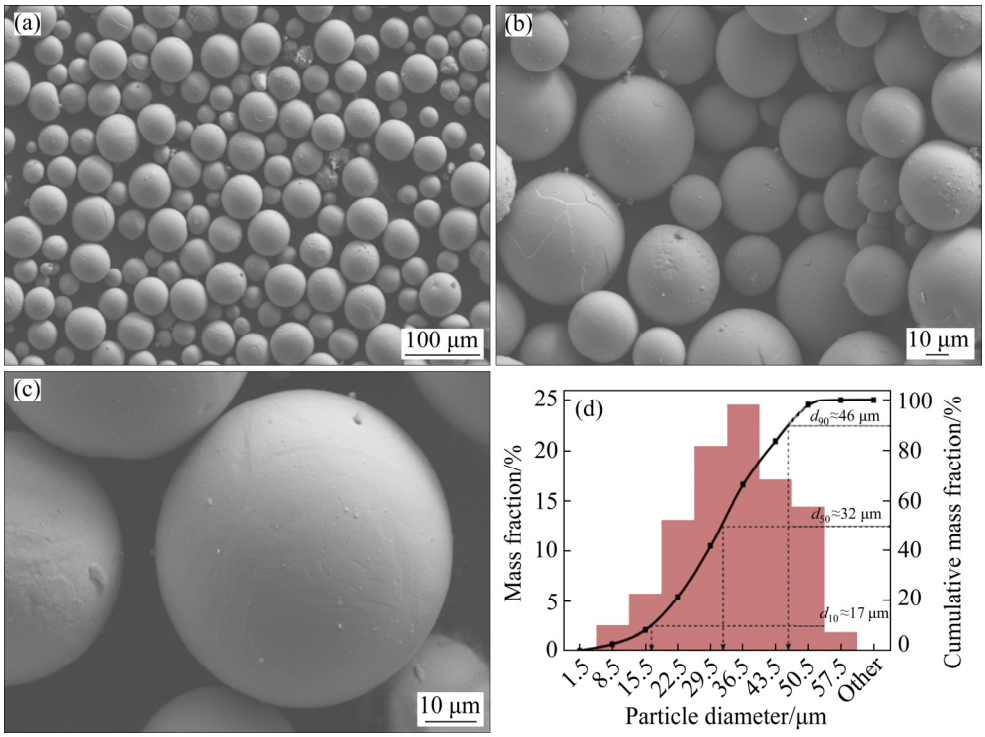

Fig. 9 SEM images at various magnification scales for powder particles (a−c) and particle size distribution (d) in size range from 0 to 53 μm

particles that the plasma jets can ensure enough heat to melt the wire and the required overheating temperature for liquid material. Another conclusion is that the power of the torches is sufficient to melt the wire and to disintegrate the liquid metal into fine spherical particles. The average powder size (d_{50}) value was approximately 32 μm in the size range of 0−53 μm. According to the cumulative size distribution curve, 90% of the particles are less than 46 μm and 10% of the particles are less than 17 μm. Furthermore, when the powder size distribution and shape properties are examined, it is shown that the powders obtained are suitable for selective laser melting, powder injection molding, and hot isostatic pressing methods.

Figure 10 shows SEM images of powder particles in the size range from 53 to 125 μm and their particle size distribution curve. The average powder size (d_{50}) value in this size range was approximately 68 μm. According to the cumulative size distribution curve, 90% of the particles were below 98 μm, and 10% were below 53 μm. Also, hard layers on the particle surfaces were detected, as shown in this figure. It was thought that the surface of these particles (indicated by arrows) that cooled faster and were coated with a harder layer, was exposed to thermal stresses. Similar images were also available in scientific studies [15−18] with powders from manufacturers.

In order to produce powders with fine powder size, the temperature and velocity values to be obtained from the torches should be as high as possible. With the increasing torch power, the temperature and velocity values of the plasma jet also increase. By using the CD nozzle attachment, sufficient velocity values are achieved for efficient fragmentation. Similarly, increasing the volumetric flow values of the plasma gas increases the plasma jet velocity. At the same time, since the gas/metal flow rate is an important issue in controlling the size in the atomization process, an increase in this ratio is the parameter that controls the produced powder size. In controlling the powder size in the plasma atomization process, not only the torch power, but also the temperature and velocity of the plasma jet, as well as the distance of intersection with the wire, are important.

Figure 11 shows the particle size distributions of the powders, which were previously made with high power and produced using low power within the scope of this study. In this way, a comparison of powders produced by other methods was also made. Accordingly, it is seen that the cumulative powder size curves using low-power and high-power curves are similar. According to the graph (Curves (e) and (f)), only 15% of the powders produced by PREP

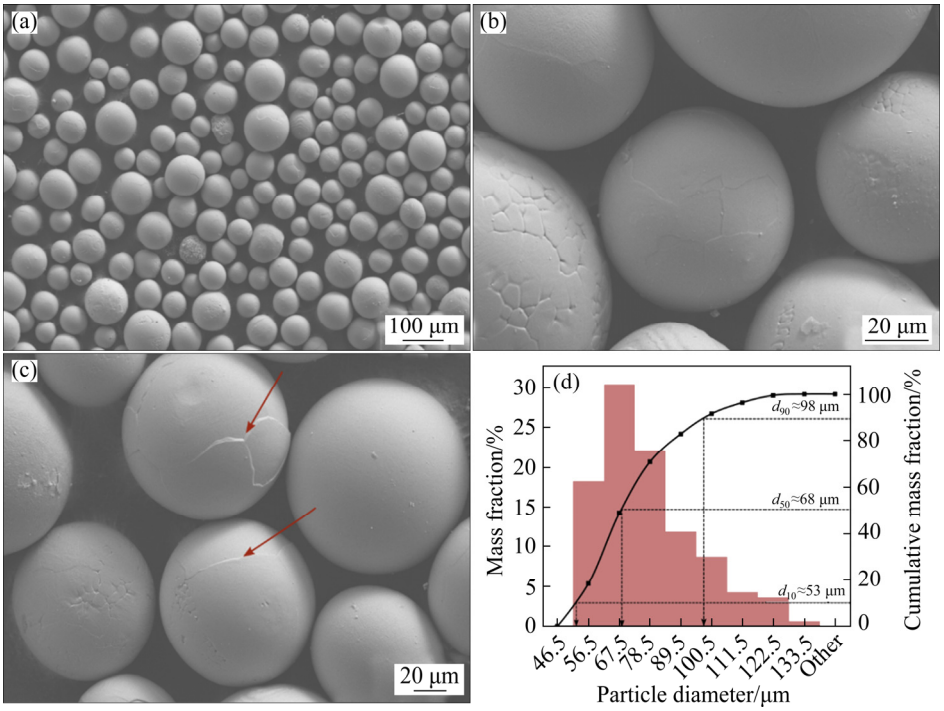

Fig. 10 SEM images at various magnification scales for powder particles (a−c) and particle size distribution (d) in size range from 53 to 125 μm

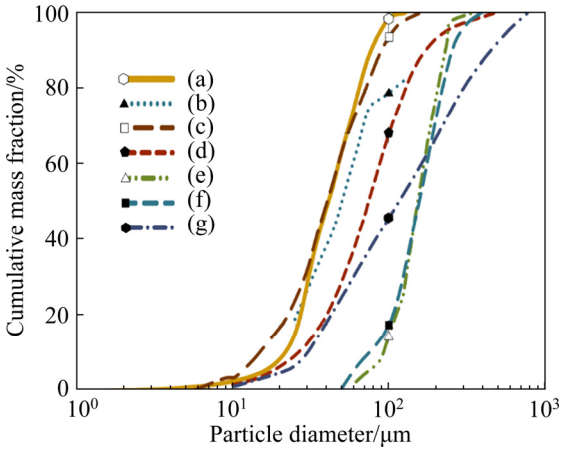

Fig. 11 PSD graphs of Ti−6Al−4V powders produced by PA and different methods: (a) This study; (b) PA [19]; (c) PA [20]; (d) EIGA [19]; (e) PREP [19]; (f) PREP [20]; (g) Argon atomizer [20]

method consist of powders of 100 μm and below. This method is consistent with previous studies [21] in which coarser powders are produced [22,23], but are formally similar to PA in terms of their excellent sphericity, the lack of gas-filled pores. 45% of argon atomized powders (Curve (g)) are composed of 100 μm particles. Due to the shape [24] and gas porous voids [25] of these powders, they are not particularly preferred in processes such as AM. It is also inefficient in cost as it uses higher energy than other methods in powder production, especially from reactive materials with a high melting temperature. 68% of EIGA powders (Curve (d)) are composed of 100 μm particles. Although it is considered to be positive in terms of particle-size distribution (PSD), satellite formation, porous structure [26], and high gas consumption [27] are among the disadvantages of the method. Curves (b) and (c) in Fig. 11 show two different powders produced with PA. Accordingly, Curve (b) shows that the sizes of 79% the powders are 100 μm. Curve (c) shows that the sizes of 94% powders are not larger than 100 μm. 98% of the powders produced within the scope of this study (Curve (a)) consist of 100 μm particles.

In Fig. 12, a microstructure examination of the particles smaller than 53 μm was performed. Figure 12(b) shows the microstructure of particles obtained after etching. Accordingly, the structure formed was dominated by the martensitic α phase due to the high cooling rate (10^3 to 10^5 K/s) in the atomization process. These structures appear to be needle-like. The white layer on the outer wall of the particle is thought to be the primary β boundary

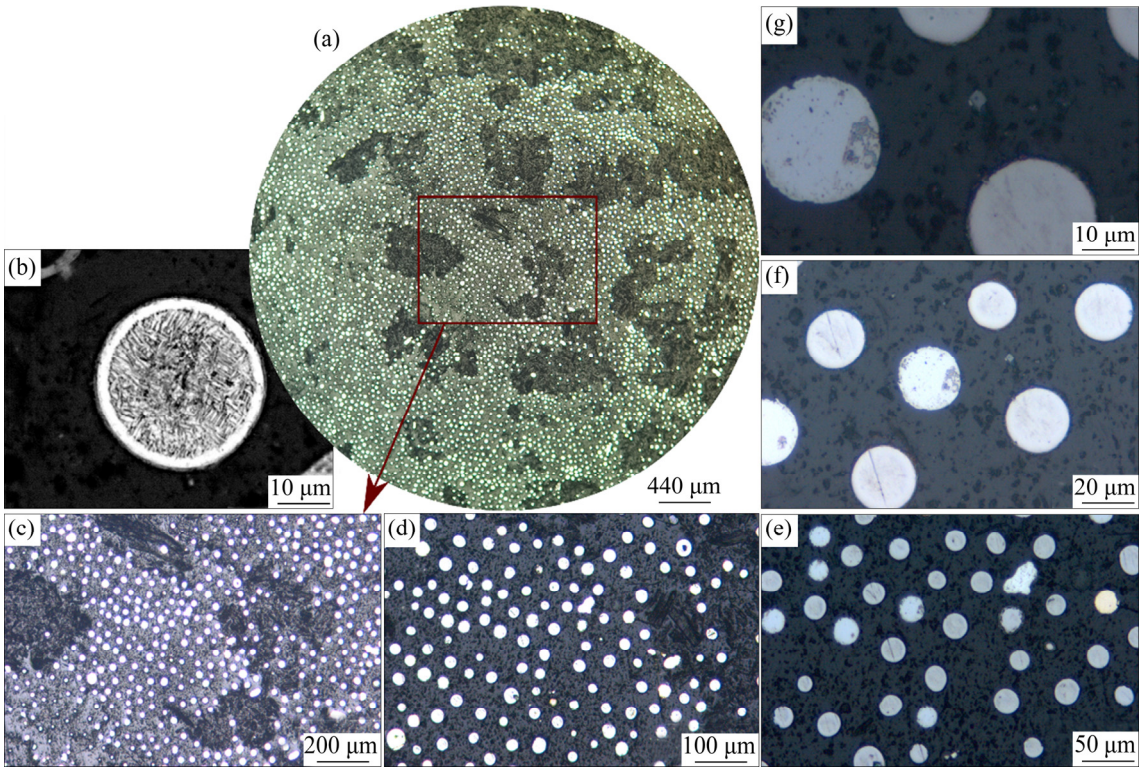

Fig. 12 Microstructures of particles in size range of 0−53 μm: (a) General view; (b) Etched; (c−g) Different magnification scales without etching

formed by rapid solidification towards the center of the particle. Similar images have been observed in other scientific studies [18,28,29]. Figures 12(c−g) show images at various magnification scales of metallographically examined particles without the etching process. It is shown clearly that the sphericity of the particles is quite good.

In Fig. 13, a microstructure examination of the particles in the size range of 53 to 125 μm was performed. Figure 13(b) shows the image obtained with the etching of the particle. The martensitic α phase was dominant appearing as needle-like structures. The plasma jets melted the wire and disintegrated the melt into small droplets. After spheroidization of droplets, they cooled rapidly and produced a martensitic surface layer on the particles. Figures 13(c−g) show the interior of the particles subjected to metallographic examination at various magnification scales. Particles were solid, and there was almost no internal porosity in this size range.

Figure 14 shows an examination of pore formation at various magnifications for different powder size ranges. It is seen from the figure that there are almost no pores in powders in the 0 to 53 μm and 53 to 125 μm size ranges, but there are some pores in coarser particles. It is thought that these pores are argon-filled pores that are used in production. The dimensions of the pores formed in the coarser particles are in the range from 0 to 100 μm and spherical in shape.

4.5 Comparison of production using commercial powders

Scientific studies in published literature consist of studies on powders supplied from manufacturers. Figures 15(a) and (b) are images obtained by examination of powders from commercial powder producers. Figure 15(c) shows powder image presented in a scientific study [30]. Figures 15(d−f) are pictures of powders produced in this study. Although the shapes of both powder samples are quite spherical, there are some exceptions. The sphericity of the powder particles produced in this study was very successful, and they are comparable to commercial powders.

According to the images given in Fig. 16, the plasma-atomized powder can be comparable with plasma rotating electrode process (PREP) powders in terms of shape. Although they had a rather spherical structure, powders are generally coarse. For this purpose, the PA method is superior to other

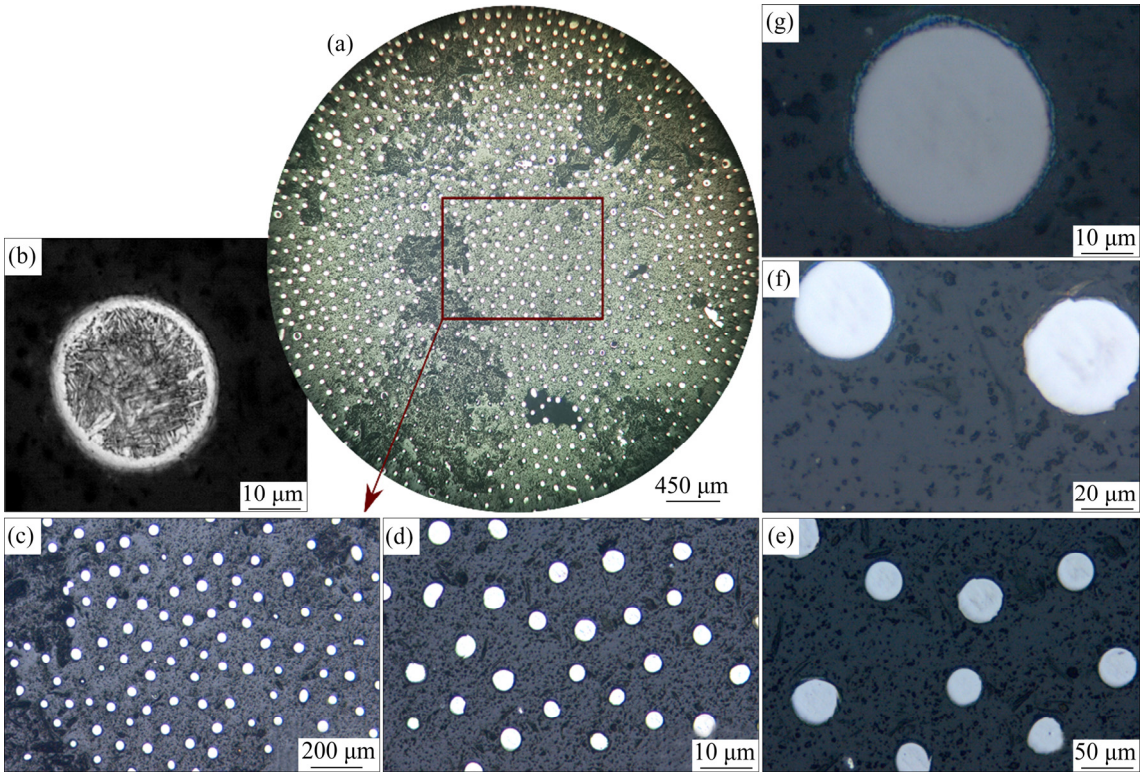

Fig. 13 Microstructures of particle in size range of 53−125 μm: (a) General view; (b) Etched; (c−g) Different magnification scales without etching

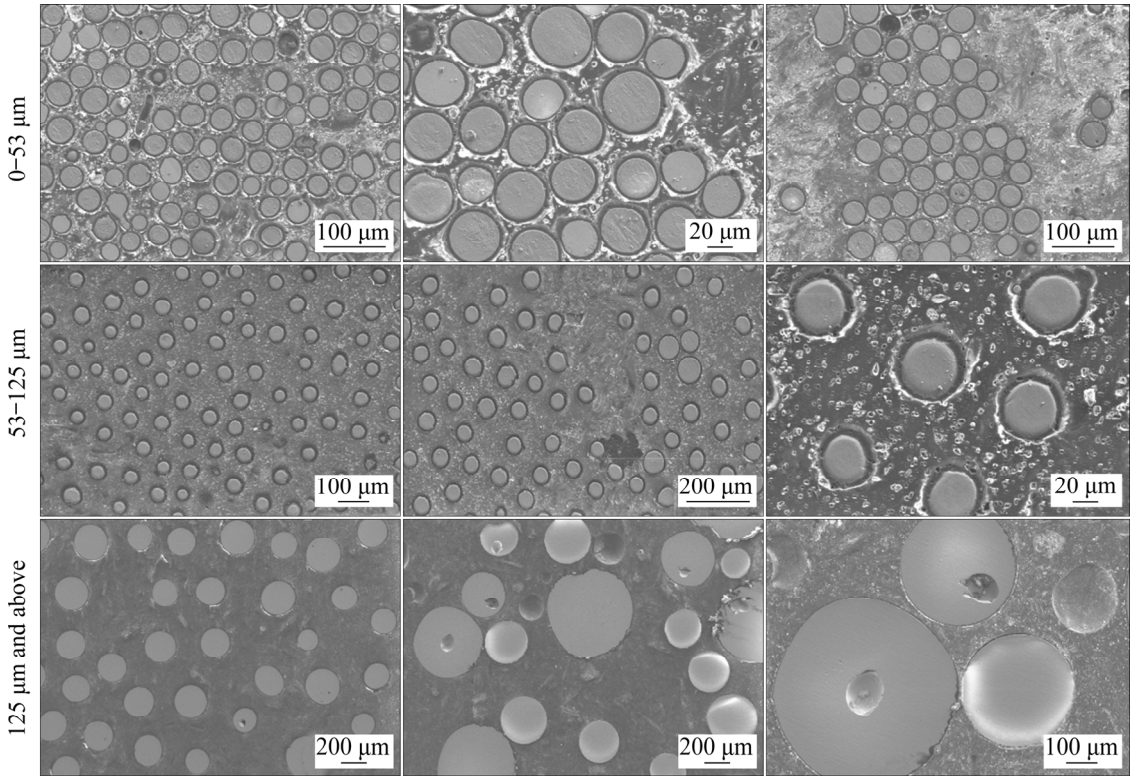

Fig. 14 Examination of gas pores in particles of different particle size ranges

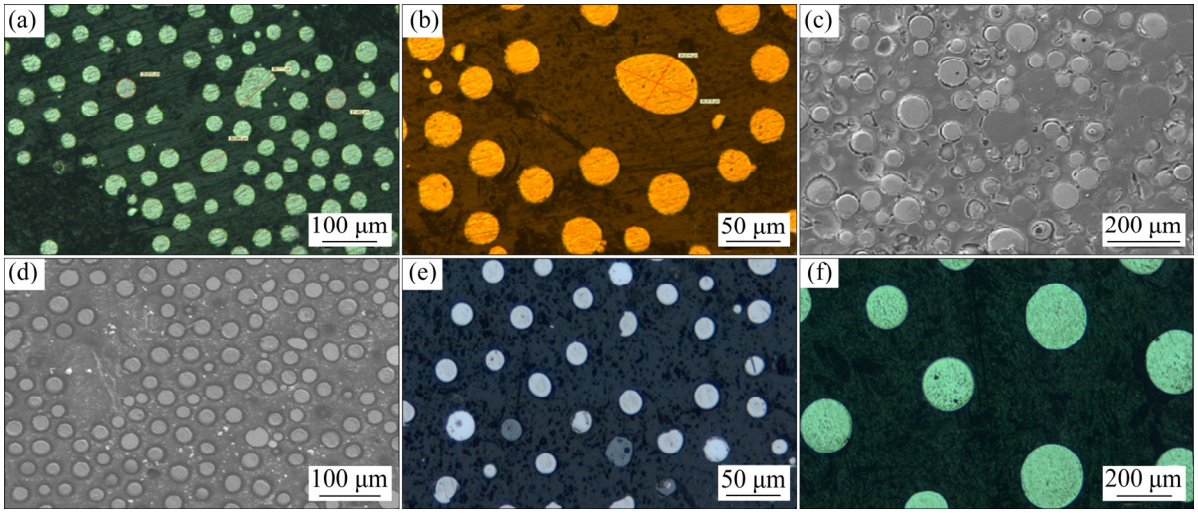

Fig. 15 Images of plasma-atomized powders from commercial producers (a, b), powders in Ref. [30] (c) and powders produced in this study (d−f)

methods in terms of intracellular porosity, shape, size, and microstructural properties. The images of the powders produced in this study at various magnifications are given as a separate column on the right-hand side of Fig. 16 [19,24,26,30−32]. It is thought that the powder properties produced on the laboratory scale plasma atomization setup with low torch power are comparable to properties of commercial powders produced by the same method.

5 Conclusions

(1) A high velocity nozzle attachment was necessary to assemble three torches to ensure a short distance between the torch exit and the apex of the plasma jets. It also increased the velocity of the plasma jet for more complete atomization.

(2) The wire temperature reached its highest

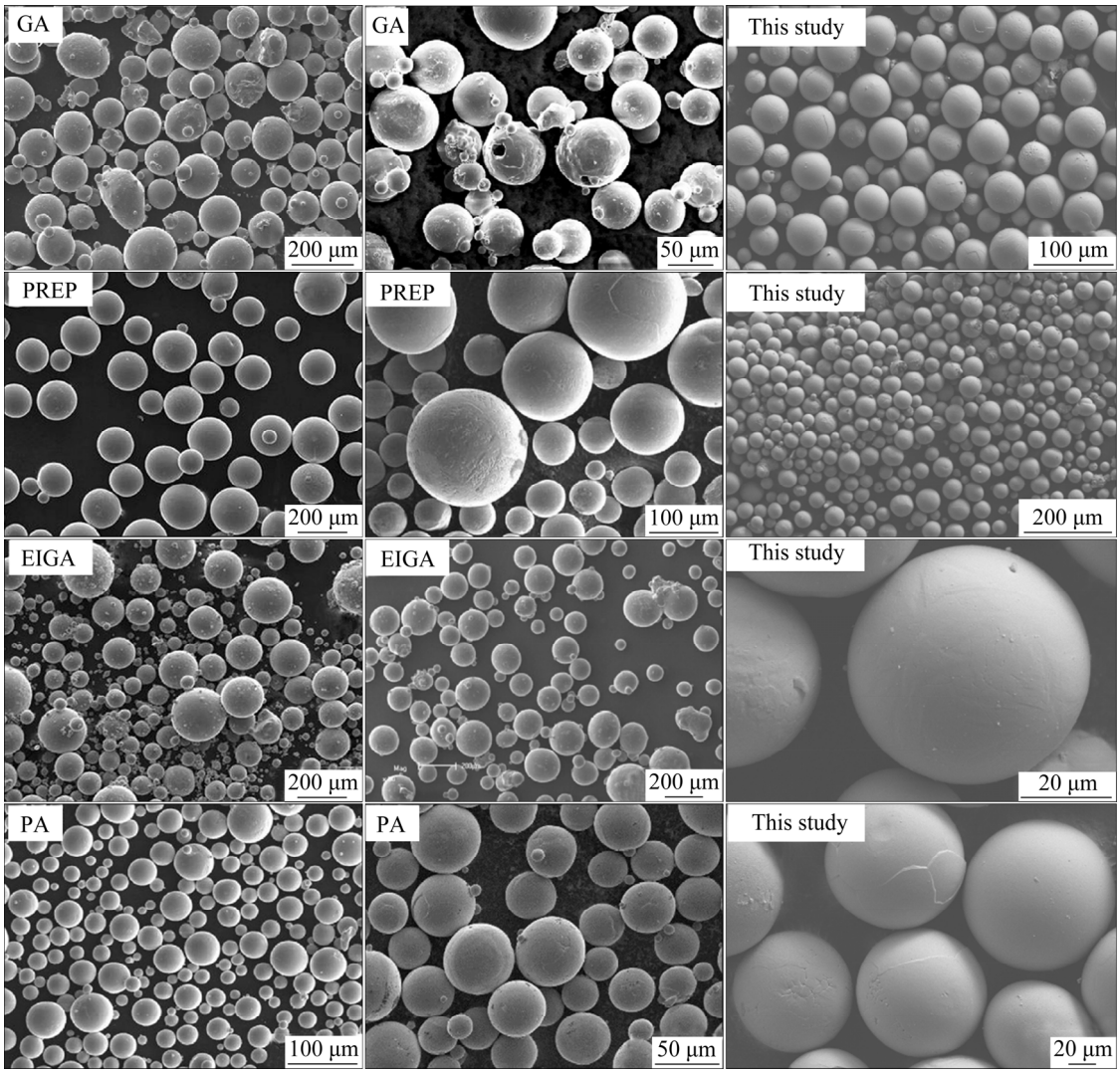

Fig. 16 Comparison of different powders produced by plasma atomization and other methods in terms of shape properties (References: [24,30] for GA; [19,31] for PA; [19,26] for PREP; [26,32] for EIGA)

value at about 10 mm above the apex of the jets. For 60, 70, and 90 L/min flow rates, temperatures at the apex were 11575.89, 11234.42, and 10636.32 K, respectively. This result showed that plasma jets are suitable for the atomization of Ti alloy.

(3) The addition of the high velocity nozzle attachment increased the plasma jet velocity to the required level; however, it caused a decrease in the plasma jet temperature. The highest velocities inside the nozzle attachment were between 838 and 1178 m/s. The velocities of the jets at the apex were between 494 and 645 m/s for different gas flow rates. These velocities were enough to disintegrate the melt into fine droplets.

(4) The studied plasma gas flow rates had no significant effect on the effective plasma jet length. It was shown that the plasma jet length can be estimated by numerical analysis using the temperature and velocity change of the plasma jet over distance.

(5) The powders produced on the laboratory scale in this study can compete with the commercial powders in terms of sphericity, particle size and microstructural properties.

Acknowledgments

The authors are grateful for the financial supports from the Scientific and Technological Research Council of Turkey (No. 215M895).

References

[1] FU Peng-huai, WANG Nan-qing, LIAO Hai-guang, XU Wen-yu, PENG Li-ming, CHEN Juan, HU Guo-qi, DING Wen-jiang. Microstructure and mechanical properties of

high strength Mg−15Gd−1Zn−0.4Zr alloy additive-manufactured by selective laser melting process [J]. Transactions of Nonferrous Metals Society of China, 2021, 31: 1969−1978.

[2] MEIER C, WEISSBACH R, WEINBERG J, WALL W A, HART A J. Critical influences of particle size and adhesion on the powder layer uniformity in metal additive manufacturing [J]. Journal of Materials Processing Technology, 2019, 266: 484−501.

[3] GAO Chao-feng, XIAO Zhi-yu, ZOU Hai-ping, LIU Zhong-qiang, CHEN Jin, LI Shang-kui, ZHANG Da-tong. Characterization of spherical AlSi10Mg powder produced by double-nozzle gas atomization using different parameters [J]. Transactions of Nonferrous Metals Society of China, 2019, 29: 374−384.

[4] SUN P, FANG Z Z, XIA Y, ZHANG Y, ZHOU C. A novel method for production of spherical Ti−6Al−4V powder for additive manufacturing [J]. Powder Technology, 2016, 301: 331−335.

[5] LAROUCHE F, BALMAYER M, TRUDEAU-LALONDE F. Plasma atomization metal powder manufacturing processes and systems therefore: US patent, 20180214956A1 [P]. 2018−08−02.

[6] BOULOS M I, JUREWICZ J W, AUGER A. Process and apparatus for producing powder particles by atomization of a feed material in the form of an elongated member: WIPO patent, 2015/135075 A1 [P]. 2015−09−15.

[7] TSANTRIZOS P G, ALLAIRE F, ENTEZARIAN M. Method of production of metal and ceramic powders by plasma atomization: US patent, 5707419 [P]. 1998−01−13.

[8] DUMITRAS C G, CERNAT R, STAMATE T, VARDAVOULIAS M. Study on high-purity titanium powder for biomedical application [J]. Journal of Optoelectronics and Advanced Materials, 2014, 16: 1447−1455.

[9] SELVAN B, RAMACHANDRAN K, SREEKUMAR K P, THIYAGARAJAN T K, ANANTHAPADMANABHAN P V. Numerical and experimental studies on DC plasma spray torch [J]. Vacuum, 2009, 84: 444−452.

[10] GUO Z W, YIN S, LIAO H L, GU S. Three-dimensional simulation of an argon-hydrogen DC non-transferred arc plasma torch [J]. International Journal of Heat and Mass Transfer, 2015, 80: 644−652.

[11] GUO Kuai-kuai, LIU Chang-sheng, CHEN Sui-yuan, DONG Huan-huan, WANG Si-yu. High pressure EIGA preparation and 3D printing capability of Ti−6Al−4V powder [J]. Transactions of Nonferrous Metals Society of China, 2020, 30: 147−159.

[12] MURPHY A B, UHRLANDT D. Foundations of high-pressure thermal plasmas [J]. Plasma Sources Science and Technology, 2018, 27: 1−20.

[13] BENJAMIN D, KIRKPATRICK C W. Properties and selection: Stainless steels, tool materials and special purpose metals [M]. 9th ed. New York: ASM International, 1980.

[14] VAJPAI S K, OTA M, WATANABE T, MAEDA R, SEKIGUCHI T, KUSAKA T, AMEYAMA K. The development of high performance Ti−6Al−4V alloy via a unique microstructural design with bimodal grain size distribution [J]. Metallurgical and Materials Transactions A, 2014, 46: 903−914.

[15] SEYDA V, HERZOG D, EMMELMANN C. Relationship between powder characteristics and part properties in laser beam melting of Ti−6Al−4V and implications on quality [J]. Journal of Laser Applications, 2017, 29: 1−8.

[16] KIM Y, KIM E P, SONG Y B, LEE S H, KWON Y S. Microstructure and mechanical properties of hot isostatically pressed Ti−6Al−4V alloy [J]. Journal of Alloys and Compounds, 2014, 603: 207−212.

[17] CHENA J, DENG H, CHEN L Q, WEI Y Q, XIA Z, TANG J. Structure and mechanical properties of low doped-Zr TC4 alloy prepared by spark plasma sintering [J]. Advanced Engineering Materials, 2018, 20: 1−8.

[18] BIRT A M, CHAMPAGNE V K, SISSON R D, APELIAN D. Microstructural analysis of Ti−6Al−4V powder for cold gas dynamic spray applications [J]. Advanced Powder Technology, 2015, 26: 1335−1347.

[19] SUN P, FANG Z G, ZHANG Y, XIA Y. Review of the methods for production of spherical Ti and Ti alloy powder [J]. The Journal of the Minerals, Metals & Materials Society, 2017, 69: 1853−1860.

[20] ENTEZARIAN M, ALLAIRE F, TSANTRIZOS P, DREW R A L. Plasma atomization: A new process for the production of fine, spherical powders [J]. JOM, 1996, 48: 53−55.

[21] CAPUS J. AP&C: Moving fast with the rise of AM [J]. Metal Powder Report, 2017, 72: 22−24.

[22] VAJPAI S K, AMEYAMA K. A novel powder metallurgy processing approach to prepare fine-grained Ti-rich TiAl-based alloys from pre-alloyed powders [J]. Intermetallics, 2013, 42: 146−155.

[23] YAMANOGLU R, GERMAN R M, KARAGOZ S, BRADBURY W L, ZEREN M, LI W, OLEVSKY E A. Microstructural investigation of as cast and PREP atomised Ti−6Al−4V alloy [J]. Powder Metallurgy, 2011, 54: 604−607.

[24] AHSAN M N, PINKERTON A J, MOAT R J, SHACKLETON J. A comparative study of laser direct metal deposition characteristics using gas and plasma-atomized Ti−6Al−4V powders [J]. Material Science and Engineering A, 2011, 528: 7648−7657.

[25] CHEN Y, ZHANG J Y, WANG B, YAO C G. Comparative study of IN600 superalloy produced by two powder metallurgy technologies: Argon atomizing and plasma rotating electrode process [J]. Vacuum, 2018, 156: 302−309.

[26] GUO R P, XU L, ZONG B Y, YANG R. Characterization of prealloyed Ti−6Al−4V powders from EIGA and PREP process and mechanical properties of HIPed powder compacts [J]. Acta Metallurgica Sinica, 2017, 30: 735−744.

[27] FANG Z F, PARAMORE J D, SUN P, CHANDRAN K S R, ZHANG Y, XIA Y, CAO F, KOOPMAN M, FREE M. Powder metallurgy of titanium—Past, present, and future [J]. International Materials Reviews, 2018, 63: 407−459.

[28] BIRT A M, CHAMPAGNE V K, SISSON R D, APELIAN D. Microstructural analysis of cold-sprayed Ti−6Al−4V at the micro- and nano-scale [J]. Journal of Thermal Spray Technology, 2015, 24: 1277−1288.

[29] ZHANG K, MEI J, WAIN N, WU X. Effect of hot-isostatic-pressing parameters on the microstructure and properties of powder Ti−6Al−4V hot-isostatically-pressed samples [J]. Metallurgical and Materials Transactions A, 2010, 41: 1033−1045.

[30] CHEN G, ZHAO S Y, TAN P, WANG J, XIANG C S, TANG H P. A comparative study of Ti−6Al−4V powders for additive manufacturing by gas atomization, plasma rotating electrode process and plasma atomization [J]. Powder Technology, 2018, 333: 38−46.

[31] MEIER C, WEISSBACH R, WEINBERG J, WALL W A, HART A J. Modeling and characterization of cohesion in fine metal powders with a focus on additive manufacturing process simulations [J]. Powder Technology, 2019, 343: 855−866.

[32] GUO R P, XU L, WU J, YANG R, ZONG B Y. Microstructural evolution and mechanical properties of powder metallurgy Ti−6Al−4V alloy based on heat response [J]. Materials Science and Engineering A, 2015, 639: 327−334.

低功率等离子体炬生产钛合金粉末的理论与实验研究

Emre YURTKURAN[1], Rahmi ÜNAL[2]

1. Department of Mechanical Engineering, Faculty of Engineering and Natural Sciences, Sivas University of Science and Technology, Sivas, Turkey;
2. Department of Mechanical Engineering, Faculty of Engineering, Gazi University, Ankara, Turkey

摘　要：探讨使用低功率等离子体炬生产钛合金金属粉末的可能性。设计一种氩气直流非转移电弧等离子体炬，并对其等离子体射流特性和导线温度进行数值分析。喷嘴附件内的最高射流速度为 838~1178 m/s，不同气体流速下顶点处的射流速度为 494~645 m/s。等离子体气体流速对有效等离子体射流长度无显著影响。利用等离子体射流的温度和速度随距离的变化，可通过数值分析预测等离子体射流的长度。所制备的粉末为球形，无卫星粉。总之，本研究开发并使用低功率等离子体炬成功生产了钛合金粉末。

关键词：等离子雾化；颗粒尺寸；粉末生产；热等离子体炬；钛合金粉末；计算流体动力学；显微组织

(Edited by Wei-ping CHEN)